AIAA 81-0144R

Experimental Aerodynamic Characteristics of Missiles with Square Cross Sections

D.C. Daniel*
Air Force Armament Laboratory, Eglin AFB, Fla.
and
T.R. Yechout† and G.J. Zollars‡
United States Air Force Academy, Colo.

Subsonic aerodynamic force and moment characteristics have been determined for a parametric family of missiles with square cross sections. Geometric variables considered in the experimental study were body cross-section corner radius, nose planform, and fin planform. Body-alone and body-fin data were obtained for angles of attack from 0 to 30 deg at roll angles of 0, 22.5, and 45 deg. Surface oil-flow patterns were also obtained. The results clearly show the strong influence of body cross-section corner radius on the aerodynamic forces and moments.

Nomenclature

b = body cross-section width (diameter)
C_A = axial-force coefficient
C_ℓ = rolling moment coefficient
C_m = pitching moment coefficient
C_N = normal-force coefficient
C_n = yawing moment coefficient
C_Y = side-force coefficient
M_∞ = freestream Mach number
r = body cross-section corner radius
V_∞ = freestream velocity
α = angle of attack
α_t = total angle of attack
ϕ = roll angle

Introduction

RECENTLY the possibility of using rectangular or square cross-section bodies as missiles or submunition dispensers has received increasing attention. This interest is due primarily to the increased internal volume that results from this type of shape as compared to missiles with circular cross sections.

Results from only a few experimental studies concerning bodies with square cross sections have been published. They include the two-dimensional work by Polhamus[1,2] and the more recent, very high angle-of-attack work by Clarkson et al.[3] In general, however, there is little in the technology base to support preliminary design or analyses of missiles with square cross sections, especially those requiring moderate amounts of maneuverability.

To assist in overcoming this deficiency, the Air Force Armament Laboratory and the Air Force Academy are conducting a two-phase research program into the aerodynamic characteristics of missiles with square cross sections. The first phase of the program is concerned with experimental force and moment measurements for a wide range of geometries, orientations, and flow conditions. Surface oil-flow patterns are also being investigated. The second phase of the program is concerned with detailed flowfield measurements. Partial results from the first phase of the above program are presented in this paper. The paper includes a brief description of the wind-tunnel facility used in the investigation, information on the wind-tunnel models, major force and moment results, representative oil-flow results, and detailed discussion of the results.

Wind-Tunnel Facility

The data for this investigation were obtained in the subsonic wind tunnel of the United States Air Force Academy.[4] This tunnel is a continuous flow, closed-circuit facility which has a test section of 2×3 ft and is capable of operation at a Mach number range of $0.04 \leq M_\infty \leq 0.35$ at atmospheric pressure. At the maximum operating condition, the tunnel is capable of obtaining a unit Reynolds number of 1.6 million/ft. The facility is used for research projects as well as educational experiments and demonstrations.

Wind-Tunnel Models

The various model components used in most of the investigation are shown on Fig. 1. This figure depicts the four bodies, each with a different cross-section corner radius; the two noses, a blunted tangent ogive and a pointed tangent ogive; and one each of the three sets of fins that were used. All components were made of aluminum.

The normalized body corner radii (r/b) values investigated were 0.0, 0.1, 0.2, and 0.5. These bodies are depicted on Fig. 1 as B1, B2, B3, and B4, respectively. Each body section was 12 in. long and had a width (diameter) of 2 in.

The blunted tangent ogive nose (N1) shown on Fig. 1 was 3 in. long. The pointed tangent ogive nose (N2) was 4 in. long.

The three sets of fins were designated as F1, F2, and F3. They had aspect ratios (based on exposed semispan) of 0.47, 0.67, and 0.34, respectively. Fins F1 and F3 had an exposed semispan of 1.25 in. and lengths of 4 and 6 in., respectively. Fin F2 had an exposed semispan of 1.5 in. and a length of 3 in. The fins were mounted in a standard cruciform arrangement at the corners of the body cross section.

In addition to the models described above, a smaller half-scale version of model N1B3F1 was also fabricated. This model was used for some scale comparison experiments in the subsonic wind tunnel, and it also will be used in future ex-

Presented as Paper 81-0144 at the AIAA 19th Aerospace Sciences Meeting, St. Louis, Mo., Jan. 12-15, 1981; submitted March 10, 1981; revision received Oct. 28, 1981.

*Research Manager. Associate Fellow AIAA.
†Major USAF, Assistant Professor of Aeronautics, Instructor of Aeronautics.
‡Captain USAF, Instructor of Aeronautics.

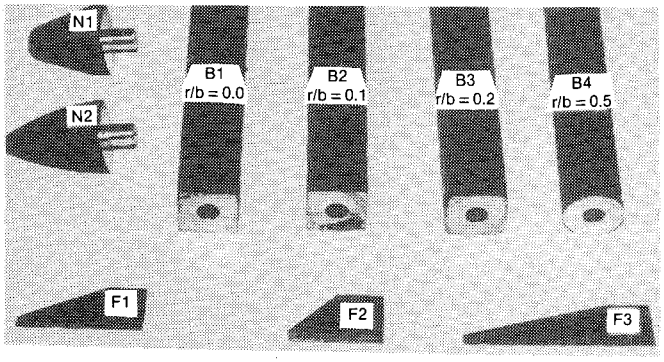

Fig. 1 Wind tunnel model components.

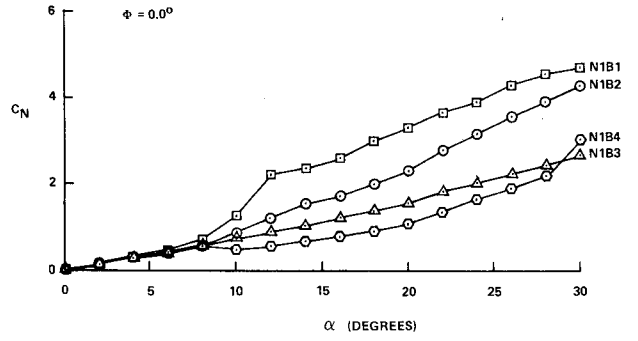

Fig. 2 Variation of body-alone normal-force coefficient with angle of attack.

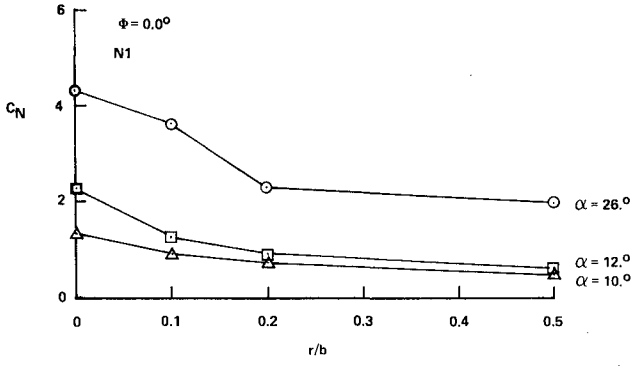

Fig. 3 Variation of body-alone normal-force coefficient with body corner radius.

periments to investigate Reynolds number and Mach number effects.

Results

The primary results obtained were six component forces and moments which were taken using an internally mounted strain gage balance. The accuracy of the balance was ±0.5% of full load output. It was mounted 6.97 in. forward from the rear of the models (3.428 in. forward for the half-scale model). All forces and moments were nondimensionalized using the base area of the body with the circular cross section (B4).

The six-component data were taken in 2-deg increments from 0 to 30 deg total angle of attack at roll orientations of 0, 22.5, and 45 deg. The freestream Mach number was approximately 0.3 for all tests; the unit Reynolds number was approximately 1.3 million/ft for all tests.

Body-alone force and moment data were obtained for all nose, body, and orientation combinations. Body-fin data using nose N1 and fin F1 with all bodies, as well as body-fin

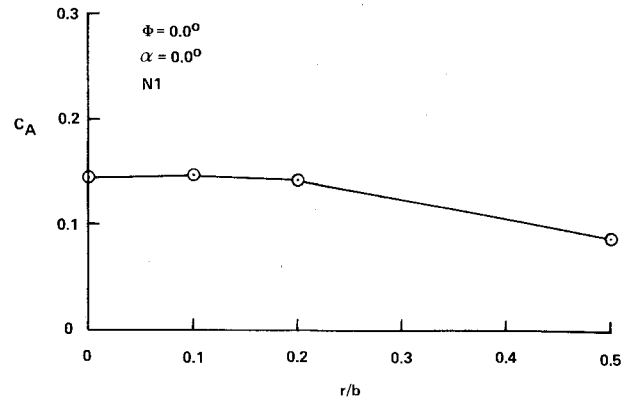

Fig. 4 Variation of body-alone axial-force coefficient with body corner radius.

data for nose N1 and body B3 with all fins, were also obtained for all orientation combinations.

In addition to the force and moment data, surface oil-flow patterns were also obtained for various body-fin combinations. These data were taken for total angles of attack of 15 and 30 deg at roll orientations of 0, 22.5, and 45 deg. A transition grit was not used for any of the experiments and the boundary layers were thought to be laminar.

Discussion of Results

Representative, major results from the wind-tunnel experiments are presented and discussed in this section of the paper. Force and moment results are presented first for the body-alone configurations, then for body-fin geometries. The section concludes with presentation and discussion of oil-flow results.

Aerodynamic Force and Moment Results

Body-Alone

Body-alone force and moment results are shown on Figs. 2-9. Figure 2 shows the variation of body-alone normal-force coefficient with angle of attack for each of the four bodies and with the blunted nose. As can be seen from this figure, the effects of body cross-section corner radius are very noticeable, particularly above 10-deg angle of attack. The normal-force coefficient for the body with the perfectly square cross section (B1) is approximately 125% higher than that for the circular body (B4) at 28-deg angle of attack. It is also interesting to note that at the higher angles of attack, the normal-force coefficients of the body with the normalized corner radii of 0.2 (B3) are close in value to the circular body (B4), whereas the values for the body with normalized corner radii of 0.1 (B2) are closer to the perfectly square body (B1). This nonlinear behavior is depicted further in Fig. 3, which shows the variations of body-alone normal-force coefficient with body corner radius for discrete angles of attack of 10, 12, and 26 deg.

The body cross-section corner radius also has a slight effect on axial-force coefficient, as shown on Fig. 4. As can be seen from this figure, the axial-force coefficient decreases with increasing corner radius. This is due primarily to the fact that the frontal area is also decreasing with increasing cross-section corner radius.

The variation of body-alone side-force coefficient with angle of attack is shown on Fig. 5. As would be expected for circular cross-section bodies of the fineness ratio investigated here, there is little evidence of side force buildup at the higher angles of attack, with the exception of body N1B1. This is the perfectly square body ($r/b = 0.0$). It has a side-force coefficient of approximately 0.5 at 30-deg angle of attack. This value is approximately 10% of the normal-force coefficient generated by this body at that angle of attack and is felt to be of little significance.

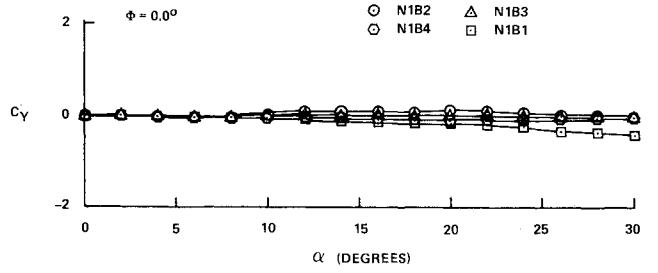

Fig. 5 Variation of body-alone side-force coefficient with angle of attack.

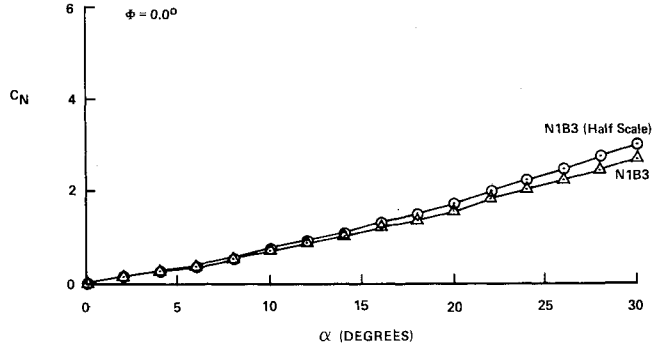

Fig. 6 Scale effects on body-alone normal-force coefficient.

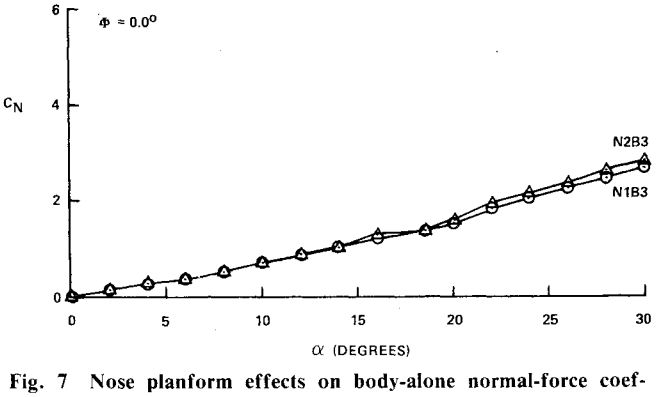

Fig. 7 Nose planform effects on body-alone normal-force coefficients.

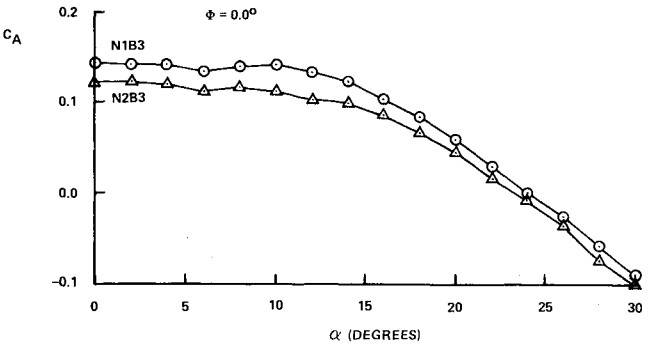

Fig. 8 Nose planform effects on body-alone axial-force coefficient.

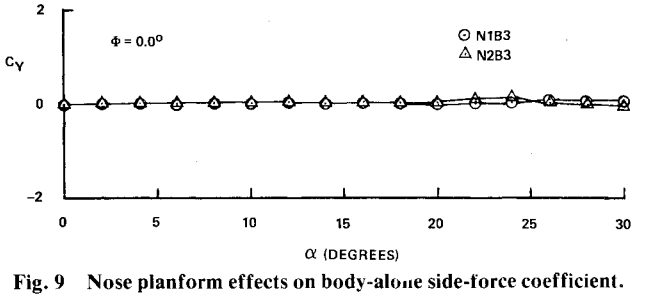

Fig. 9 Nose planform effects on body-alone side-force coefficient.

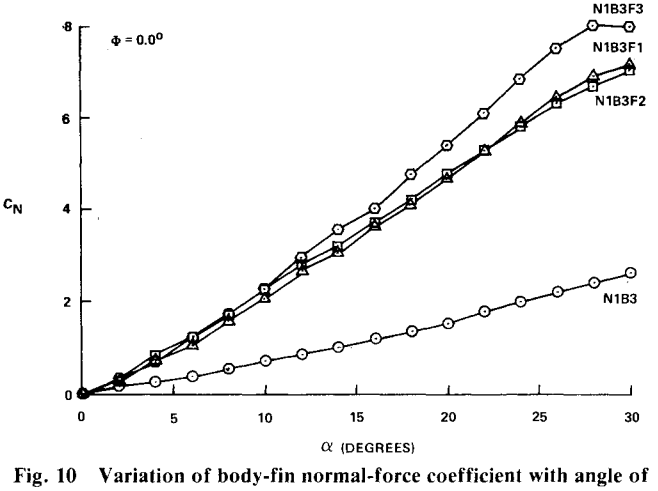

Fig. 10 Variation of body-fin normal-force coefficient with angle of attack.

An interesting scale effect result is given on Fig. 6. This figure depicts the variation of body-alone normal-force coefficient with angle of attack for body N1B3 and the half-scale equivalent of this body. The normal-force coefficient for the half-scale model is increasingly larger from approximately 6-deg angle of attack upward. This is probably due to the fact that the separating boundary layer does not scale geometrically as the models do.

Some effects of nose planform on the body-alone aerodynamics are shown on Figs. 7-9. Figure 7 shows the variation in normal-force coefficient with angle of attack for the blunted and pointed tangent ogive noses affixed to body B3. The longer pointed nose results in a slightly higher normal force at the higher angles of attack. Figure 8 shows the variation in axial-force coefficient with angle of attack for the two noses. The trends are as expected, with the sharp-nosed body having a lower value at zero angle of attack and the difference between them diminishing as angle of attack increases. Finally, the variation in side-force coefficient with angle of attack for the two noses is shown in Fig. 9. There is essentially no difference in the two results.

Body-Fin

Body-fin force and moment results are shown in Figs. 10-13. Figure 10 shows the variation of body-fin normal-force coefficient with angle of attack for each fin combination affixed to the same body. The body-alone values of normal-force coefficient are also shown for reference. As can be seen from the results on Fig. 10, the body-fin combination N1B3F3 produces the highest value of normal-force coefficient for the configurations presented on this figure. This is due to the fact that fin F3 has the largest planform area. Fins F1 and F2, having essentially the same area as each other, produce essentially the same results, albeit lower than F3.

Some interesting effects of the body cross-section corner radius for body-fin combinations are shown on Fig. 11. In this case, results are presented for configurations having the same nose (N1) and fins (F1), but affixed to bodies of different cross-section corner radius. As was the case for the body-alone results, the perfectly square body (B1) produces higher values of normal-force coefficient at the higher angles of attack than the other bodies. It is very interesting to note,

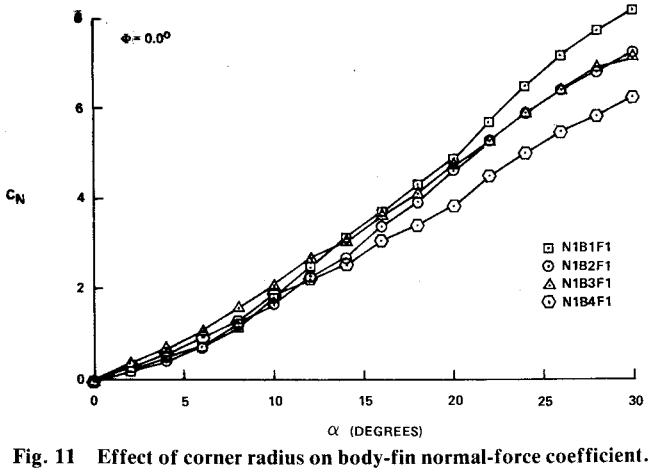

Fig. 11 Effect of corner radius on body-fin normal-force coefficient.

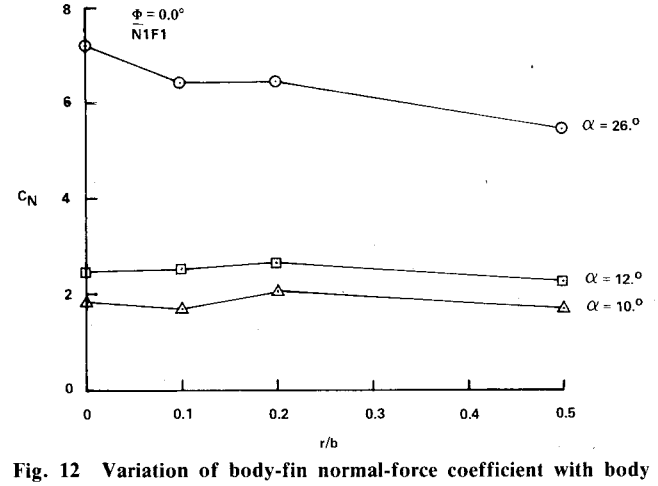

Fig. 12 Variation of body-fin normal-force coefficient with body corner radius.

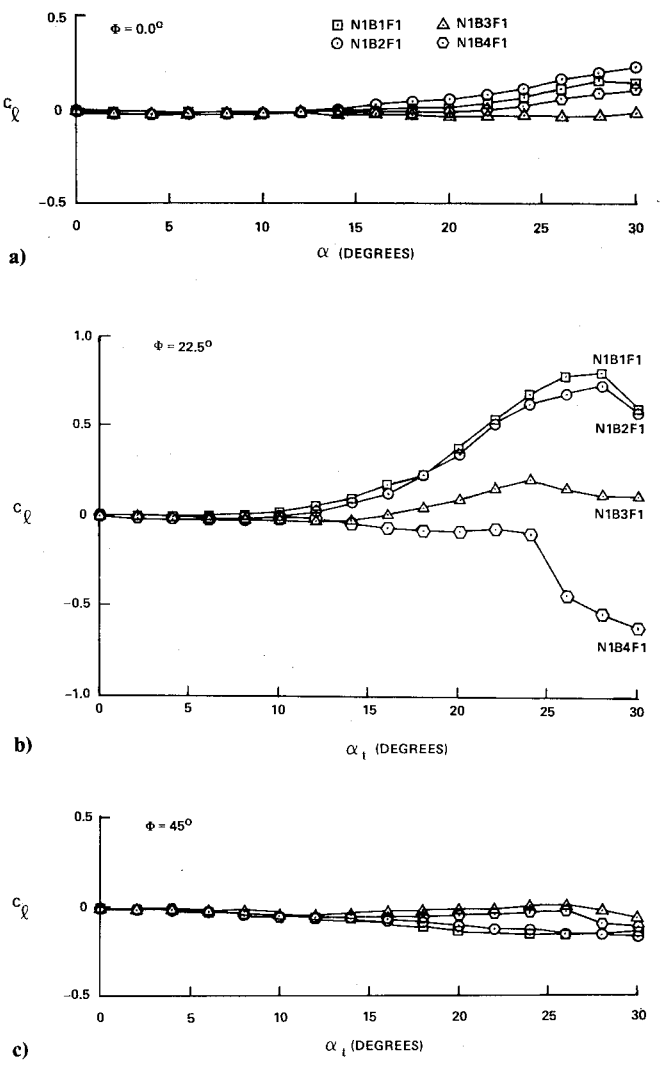

Fig. 13 a) Variation of body-fin rolling moment coefficient with total angle of attack ($\phi = 0.0$ deg); b) Variation of body-fin rolling moment coefficient with total angle of attack ($\phi = 22.5$ deg); c) Variation of body-fin rolling moment coefficient with total angle of attack ($\phi = 45.0$ deg).

however, that the variation from body to body is not nearly as pronounced as it was in the body-alone case (Fig. 2). The fins, being a major lift producing device, tend to reduce significantly the effects of corner radius on normal-force coefficient for body-fin geometries. This is demonstrated further on Fig. 12, where variations of body-fin normal force with body cross-section corner radius are shown for three discrete angles of attack.

The final aerodynamic force and moment results are presented on Fig. 13. These results show the variation in rolling-moment coefficient with total angle of attack for fixed roll angles of 0, 22.5, and 45 deg. The vehicle geometries considered are again the nose, N1, and fins, F1, affixed to bodies of different cross-section corner radius. As can be seen from these results, the corner radii have some small effect on the rolling moment at the higher angles of attack when the vehicle has a symmetric roll orientation, i.e., 0 or 45 deg. The effect for the asymmetric roll orientation ($\phi = 22.5$ deg), as shown on Fig. 13, is pronounced. For this condition, the rolling moment for the configurations with the more square bodies (N1B1F1 and N1B2F1) is large at the high angles of attack and has a positive sign. The rolling-moment coefficient for configuration N1B3F1, which has a normalized body cross-section corner radius of 0.20, stays near zero throughout the angle-of-attack range. The configuration with the circular-body cross section, N1B4F1, has a rolling moment completely unlike the others; at the higher angles of attack, it has large negative values. The reason for this strange behavior is unquestionably related to the high angle-of-attack body-separation characteristics and the immersion of the fins in leeside body vortices. As will be shown in the next section, the magnitude of the corner radius strongly affects the body separation line(s) and hence the circumferential location of the body vortices.

Surface Oil-Flow Results

Surface oil-flow patterns were obtained for various body-fin configurations during the course of the experiments described in this paper. Some of the more significant of these patterns are shown on Figs. 14 and 15.

Figure 14 shows the oil-flow patterns that were obtained for the configurations with nose, N1, and fins, F1, affixed to the four bodies of different cross-section corner radius. The view of this figure is of the side of the model that would have been toward the observer when the wind-tunnel test was run. The angle of attack for these runs was 30 deg. Review of this figure reveals that the separation patterns for configurations N1B1F1 and N1B2F1 (Figs. 14a and 14b) are very similar forward of the fins. The flow seems to separate immediately as it comes around the bottom corners; then, there is a clearly defined counter-flow region on the side of each configuration, followed by a reattachment line which moves diagonally down the body from the bottom surface, near the shoulder of the nose, to the top surface just in front of the fins. The flow along the side of configuration N1B3F1 is not at all like that of the first two configurations. In this case, the flow seems to

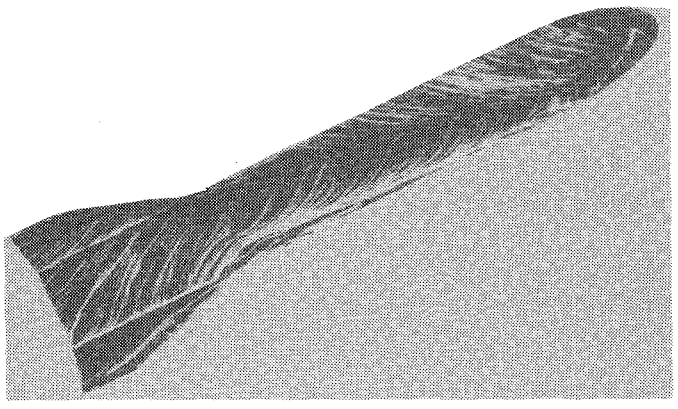

a)

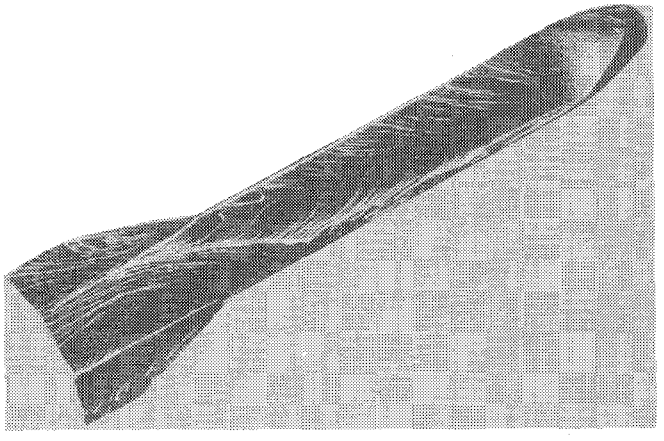

b)

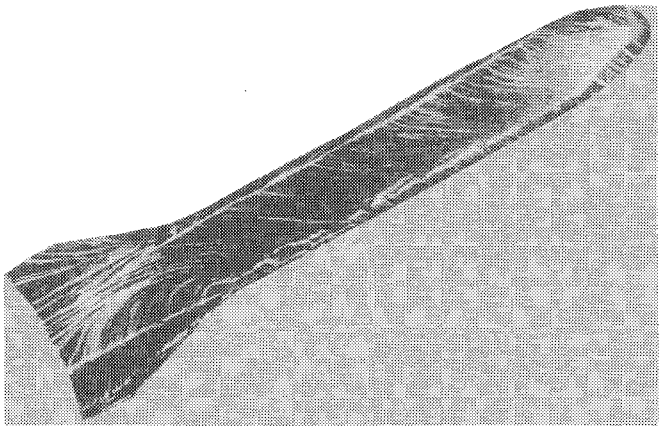

c)

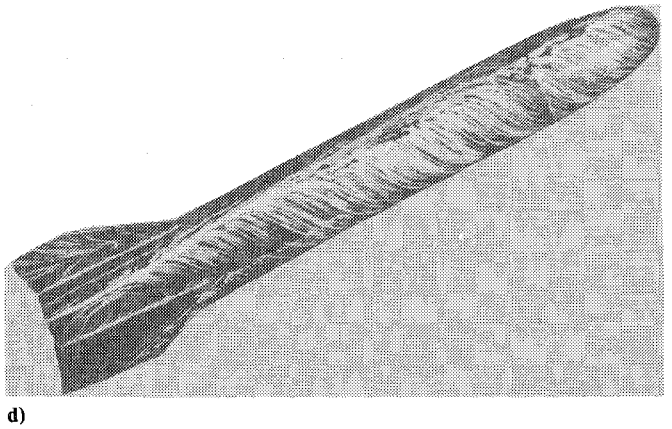

d)

Fig. 14 a) Oil-flow patterns for $\alpha_t = 30$ deg, $\phi = 0$ deg (N1B1F1); b) Oil-flow patterns for $\alpha_t = 30$ deg, $\phi = 0$ deg (N1B2F1); c) Oil-flow patterns for $\alpha_t = 30$ deg, $\phi = 0$ deg (N1B3F1); d) Oil-flow patterns for $\alpha_t = 30$ deg, $\phi = 0$ deg (N1B4F1).

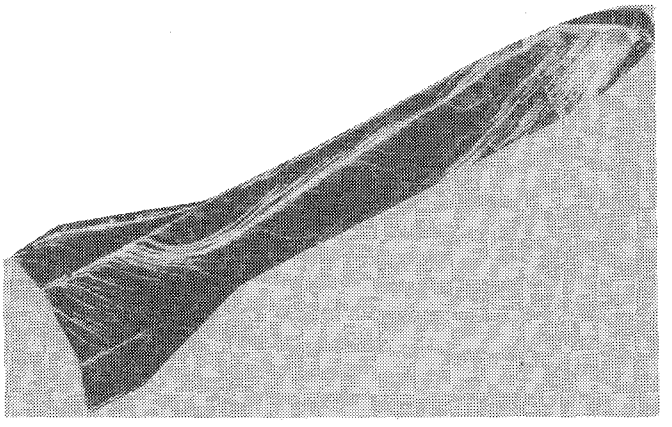

a)

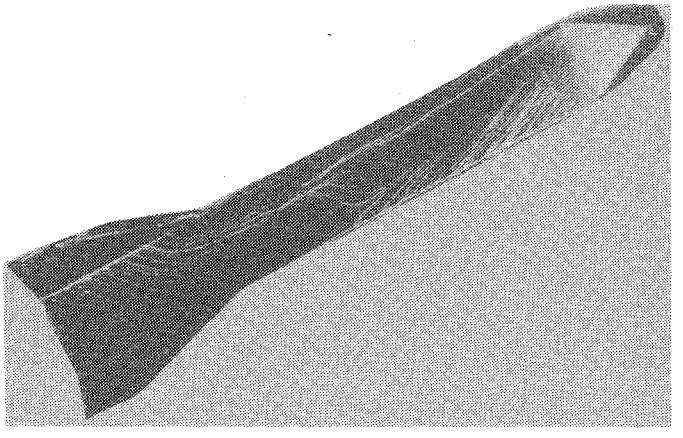

b)

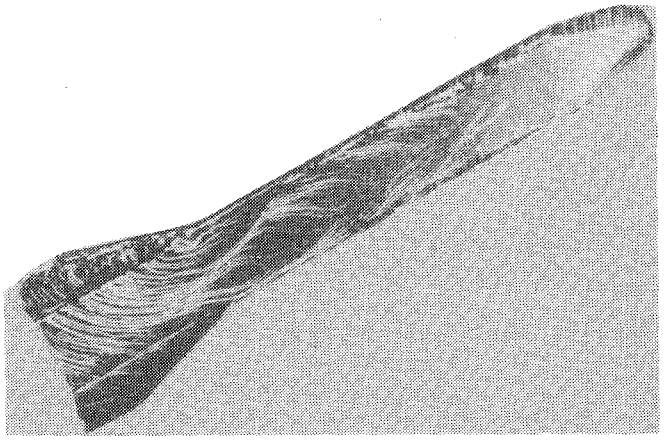

c)

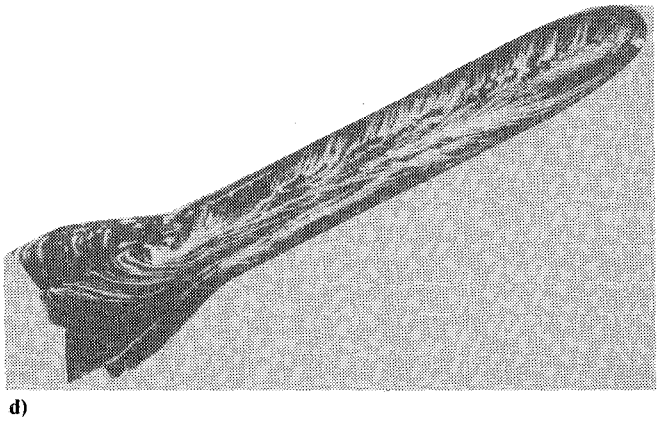

d)

Fig. 15a) Oil-flow patterns for $\alpha_t = 30$ deg, $\phi = 22.5$ deg (N1B1F1); b) Oil-flow patterns for $\alpha_t = 30$ deg, $\phi = 22.5$ deg (N1B2F1); c) Oil-flow patterns for $\alpha_t = 30$ deg, $\phi = 22.5$ deg (N1B3F1); d) Oil-flow patterns for $\alpha_t = 30$ deg, $\phi = 22.5$ deg (N1B4F1).

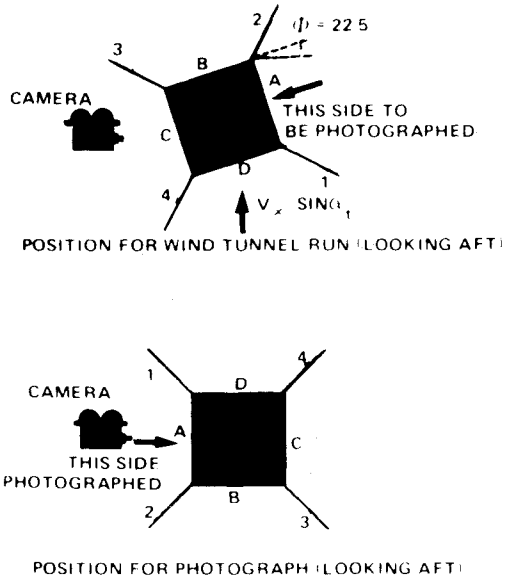

Fig. 16 Schematic of roll orientation for oil-flow patterns ($\phi = 22.5$ deg).

separate and reattach almost immediately as it comes around the bottom corner. The separation pattern for the configuration with the circular cross section, N1B4F1, is as expected.

Figure 15 shows oil-flow patterns that were obtained for the same configurations and total angle of attack as above, but for a roll angle of 22.5 deg. The side of the model that is shown in this figure was photographed at the completion of the test after the model had been rolled 180 deg to facilitate the photography. To help eliminate confusion, a schematic of the cross-flow plane during and after the experiment is shown on Fig. 16. It can be seen from Figs. 15a and 15b that these two bodies again create very similar separation patterns. From this, one would expect the rolling moments for both of these models to be very similar. As was shown previously on Fig. 13b, that is the case. The separation pattern for configuration N1B3F1, as shown in Fig. 15c, is quite different from the first two configurations. The separation line is not nearly as clearly defined and appears to have moved further around the body. The net results, as shown on Fig. 13b, is a near zero rolling moment. This could be due to the fact that the body vortex essentially passes between fins 1 and 2, as shown on Fig. 16. The final oil-flow results are shown on Fig. 15d for the configuration with the circular cross section. Here the typical twin separation lines appear for bodies of this type. This totally different separation pattern has resulted in completely different rolling moment characteristics for this body at this particular orientation. This is no doubt due to completely different fin loadings that resulted from the shift in the separation lines.

Concluding Remarks

Aerodynamic force, moment, and oil-flow results have been presented for a parametric family of missiles with square cross sections. Particular attention has been given to the effects of body cross-section corner radius. This parameter has been shown to have a very strong effect on body-alone normal-force coefficient and a lesser, but still noticeable, effect on body-fin normal-force coefficient. Body cross-section corner radius was also shown to have a strong effect on the circumferential location of the body separation line at combined roll and high angle-of-attack orientations. The location of this separation line can in turn affect both the magnitude and sense of the rolling moment coefficient.

The results presented in this paper are part of a continuing research program devoted to aerodynamics of missiles with square cross sections. Future research will emphasize Reynolds number effects and flowfield measurements.

Acknowledgments

The authors wish to express their appreciation to Paul R. Mackin and Scott R. Swinsick for their assistance in preparing the figures used in this paper. We are also indebted to our colleague Dr. M.L. Rasmussen for reviewing the paper and offering valuable criticism.

References

[1] Polhamus, E.C., Geller, E.W., and Grunwald, K.J., "Pressure and Force Characteristics of Noncircular Cylinders as Affected by Reynolds Number with a Method Included for Determining the Potential Flow About Arbitrary Shapes," NASA TR R-46, 1959.

[2] Polhamus, E.C., "Effect of Flow Incidence and Reynolds Number on Low-Speed Aerodynamic Characteristics of Several Noncircular Cylinders with Applications to Directional Stability and Spinning," NASA TR R-29, 1959.

[3] Clarkson, M.H., Malcolm, G.N., and Chapman, G.T., "A Subsonic, High Angle-of-Attack Flow Investigation at Several Reynolds Numbers," *AIAA Journal*, Vol. 16, Jan. 1978, pp. 53-60.

[4] "Subsonic and Trisonic Wind Tunnel Facilities," Department of Aeronautics, United States Air Force Academy.